Fingerprinting the ship propulsion system: low hanging fruit or mission impossible?

A. Vrijdag[*+], MSc, PhD, CEng, MIMarEST,*
Y. Sang[*], MSc*

[*] *Delft University of Technology*
[+] Corresponding Author. Email: a.vrijdag@tudelft.nl

Synopsis

In this paper the concept of ship propulsion system "fingerprinting" is explored as an alternative for data driven models that require extensive measured datasets collected over long periods of ship operation. As a first exploratory step a model of a ship in bollard pull conditions is linearised and its transfer functions are determined. Subsequently limited experimental data, involving sinusoidal excitation of the system input at a wide range of frequencies, is used to determine the system parameters. The resulting parameter estimates compare well against previously determined values. Although the developed ideas are far from ready to be used on full scale, the authors believe that the approach is promising enough to be developed further towards full scale application.

Keywords: marine propulsion system; system identification; parameter identification; linear ship propulsion system model; data driven ship propulsion model

1 Introduction

Simulation models of the ship propulsion system play an increasing role, for instance in controller design and in condition monitoring. The drawback of using simulation models however is that one has to create them. Building a simulation model and determination or estimation of its parameters can be a time-consuming task, which often requires significant experience (see for recent examples Mizythras et al. (2018), Martelli and Figari (2017) and Geertsma et al. (2017)). After building, verifying and calibrating the model (Vrijdag et al. 2009) its validity can sometimes be quantified, at least for a certain domain of application. Periodic re-validation is not commonly reported, while it is known that many of the physical parameters that play a role in the performance of the ship propulsion plant are time-variant. Examples of time-variant factors are fouling of the hull and propeller, turbocharger contamination, and so on.

Data driven modelling approaches such as for instance reported by Coraddu et al. (2016) and by Cipollini et al. (2018) might offer benefit in the sense that by making use of large amounts of historical data in combination with advanced algorithms, a "superfit" model can be generated. Drawbacks of such an approach are the amount of required data, the time over which the data are to be collected and the complexity of the analysis methods themselves.

Although the data-driven approaches based on huge datasets will without doubt play an important role in the future, in this paper a propulsion system parameter identification technique based on a short (but information-rich) controlled performance test is proposed and tested on model scale, albeit in a very simplified form. The potential benefit of such a dedicated test-cycle, carried out under controlled conditions, is that it can be used to, in a relatively short time span, quantify system performance during sea acceptance trials, after periodic maintenance or following system modifications. Comparison of this fingerprint with sister ships or with previous fingerprints could potentially be used to understand the state of decay of components.

To demonstrate the idea it is chosen to focus on a model scale ship available at Delft University of Technology (DUT). To simplify the experimental setup, the focus is on bollard pull conditions, although the ideas can be extended to free sailing conditions as well.

First the non-linear system model of a ship propulsion plant including the electric DC-motor is linearized. This linearized system model is written in the form of two second order Laplace transfer functions, of which the DC-gains, poles and zeros are derived analytically. The controllable input to the system is the supply voltage and the outputs are the motor current and the motor speed.

Subsequently a correlation based method to experimentally determine the frequency domain characteristics of the model scale ship by making use of a sinusoidal input voltage of varying frequency is applied. As a final step, the unknown parameters of the transfer functions are determined based on the combination of experimentally observed poles, zeros and DC-gains and their analytical expressions.

http://doi.org/10.24868/issn.2631-8741.2018.013

At the end of the paper a possible path is given for the development of full scale ship propulsion "fingerprinting" techniques by means of system performance tests. Such a path includes simulation based research, model scale experimental research and full scale experimental research.

2 Description of the model scale ship and its simulation model in bollard pull conditions

The ship propulsion simulation model is based on a model scale ship called "Tito Neri" which is available at DUT. It is shown in Figure 1 and a detailed picture of its azimuthing thrusters is shown in Figure 2. Its main particulars are given in Table 1.

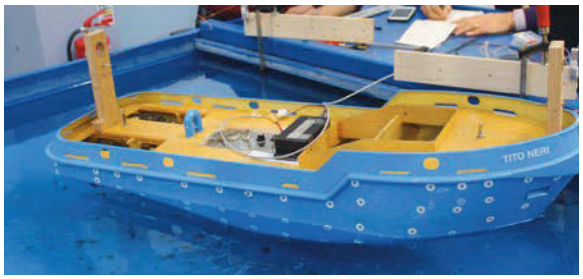

Figure 1: Tito Neri overview

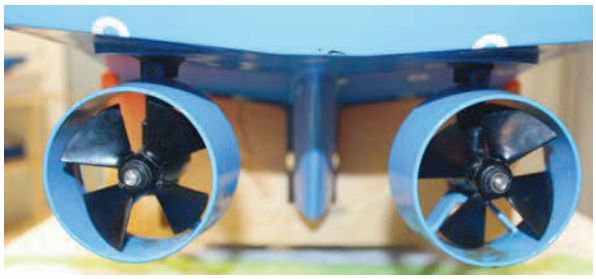

Figure 2: Tito Neri azimuthing thrusters from astern

Table 1: Main particulars Tito Neri

L_{oa}	0.97m	**Upper bevel gear teeth ratio**	13:39
B	0.32m	**Total gear reduction ratio $i_{gb,13}$**	3
Draft $T_{FPP,APP}$	0.10m, 0.13m,	**Propeller diameter D**	0.065m
Δ **(with and without battery)**	15.4kg, 13.5kg	**Number of propeller blades Z**	4

A schematic representation of one of its two drivetrains is given in Figure 3. It consists out of a DC motor that drives an azimuthing thruster with ducted fixed pitch propeller. The upper bevel gear has a reduction ratio of $i_{gb,12} = 3$ and the lower bevel gear has a reduction ratio of $i_{gb,23} = 1$.

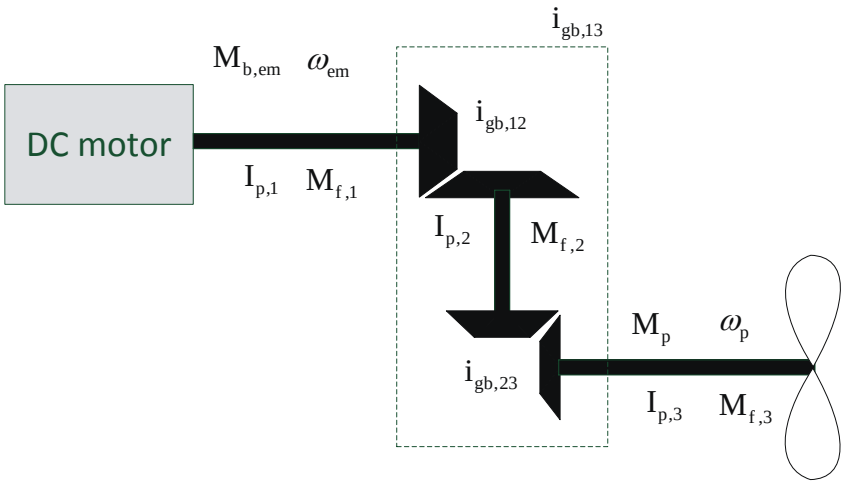

Figure 3: Schematic representation of drivetrain, including nomenclature.

Although not shown in the figure, the upper shaft is supported by a shaft bearing. The differential equation of the electric motor circuit is modelled by:

http://doi.org/10.24868/issn.2631-8741.2018.013

$$L_a \frac{di_a}{dt} = U_a - K_e \omega_{em} - R_a i_a \tag{1}$$

The reduction ratio between motor shaft and intermediate vertical shaft $i_{gb,12}$ and between intermediate vertical shaft and propeller shaft $i_{gb,23}$ and the resulting total reduction ratio $i_{gb,13}$ are defined by:

$$i_{gb,12} = \frac{\omega_{em}}{\omega_{\text{int}}}, \quad i_{gb,23} = \frac{\omega_{\text{int}}}{\omega_p}, \quad i_{gb,13} = \frac{\omega_{em}}{\omega_p} = i_{gb,12} \cdot i_{gb,23} \tag{2}$$

The differential equation for electric motor speed, assuming constant friction torque on all three shafts is given by:

$$I_{p,tot} \frac{d\omega_{em}}{dt} = M_{b,em} - M_f - \frac{M_p}{i_{gb,13}} \tag{3}$$

in which $I_{p,tot} = I_{p,1} + \frac{I_{p,2}}{i_{gb,12}^2} + \frac{I_{p,3}}{i_{gb,13}^2}$ and $M_f = M_{f,1} + \frac{M_{f,2}}{i_{gb,12}} + \frac{M_{f,3}}{i_{gb,13}}$, and in which brake electric motor torque is given by:

$$M_{b,em} = K_e \cdot i_a \tag{4}$$

The propeller torque and thrust are modelled following Carlton (2007) making use of the torque and thrust coefficients at advance ratio $J = 0$:

$$M_p = \frac{Q}{\eta_R} = \frac{K_{Q,J=0} \cdot \rho \omega_e^2 D^5}{4\pi^2 \cdot \eta_R \cdot i_{gb,13}^2} \tag{5}$$

$$T = \frac{K_{T,J=0} \cdot \rho \omega_e^2 D^4}{4\pi^2 \cdot i_{gb,13}^2} \tag{6}$$

The total bollard pull force is modelled by:

$$F_{BP} = k_p \cdot T(1-t) \tag{7}$$

where k_p is the number of propellers and the term $(1-t)$ is used to correct for thrust deduction. Based on Eqs. (1) to (7) the unknown parameters of the electric motor model are: inductance L_a, resistance R_a and motor coefficient K_e. The unknown parameters of the shaft system are: inertia $I_{p,tot}$ and friction M_f. The unknown parameters of the propeller model are: torque and thrust coefficients K_Q and K_T. The relative rotative efficiency η_R is assumed to be 1. The final unknown parameter is the thrust deduction factor t. This gives a total of 8 unknown parameters.

2.1 Linearised propulsion system model during bollard pull operation

In this section the linearised model of the ship propulsion system in Bollard Pull conditions is derived. Later on this model will be used to determine system parameters based on experiments. The linearisation process of the ship propulsion plant in free sailing mode is described in detail by Stapersma and Vrijdag (2017) and Vrijdag and Stapersma (2017), although in both papers no electric circuit including DC-motor was included. In Appendix A of this paper the linearization and normalisation approach is applied to the DC-motor driven propulsion system with ducted FPP in bollard pull condition, which results in the following two coupled normalised linear differential equations:

$$\tau_{em} \frac{di_a^*}{dt} = \frac{U_{a,0}}{U_{a,0} - K_e \omega_{em,0}} \delta U_a^* - \frac{K_e \omega_{em,0}}{U_{a,0} - K_e \omega_{em,0}} \delta\omega^* - \delta i_a^* \tag{8}$$

$$\tau_\omega \frac{d\omega_{em}^*}{dt} = \delta i_a^* - 2\eta_{trm} \delta\omega_{em}^* \tag{9}$$

in which the 2 integration constants are defined as:

http://doi.org/10.24868/issn.2631-8741.2018.013

$$\tau_{em} \equiv \frac{L_a}{R_a}, \quad \tau_{\omega} \equiv \frac{I_{p,tot}\omega_{em,0}}{M_{b,em,0}} \equiv \frac{I_{p,tot}\omega_{em,0}}{K_e i_{a,0}} \tag{10}$$

and the delta-asterisk indicates normalised difference as follows:

$$\delta i_a^* = \frac{\delta i_a}{i_{a,0}} = \frac{i_a - i_{a,0}}{i_{a,0}}, \quad \delta\omega^* = \frac{\delta\omega}{\omega_0}, \quad \delta M_{b,em}^* = \frac{\delta M_{b,em}}{M_{b,em,0}}, \quad \delta U_a^* = \frac{\delta U_a}{U_{a,0}} \tag{11}$$

such that for example a value of $\delta U_a^* = 0.05$ means a +5% perturbation from the nominal value $U_{a,0}$.

When Eqs. (8) and (9) are put in state space notation, this results in the following system:

$$\begin{bmatrix} \frac{di_a^*}{dt} \\ \frac{d\omega^*}{dt} \end{bmatrix} = \begin{bmatrix} -\frac{1}{\tau_{em}} & -\frac{1}{\tau_{em}} \cdot \frac{K_e\omega_{em,0}}{U_{a,0} - K_e\omega_{em,0}} \\ \frac{1}{\tau_{\omega}} & -\frac{2\eta_{trm}}{\tau_{\omega}} \end{bmatrix} \begin{bmatrix} \delta i_a^* \\ \delta\omega^* \end{bmatrix} + \begin{bmatrix} \frac{1}{\tau_{em}} \cdot \frac{U_{a,0}}{U_{a,0} - K_e\omega_{em,0}} \\ 0 \end{bmatrix} \delta U_a^* \tag{12}$$

The benefit of this notation is that it can easily be programmed and analysed in programs like MATLAB©. Alternatively the Laplace transfer function can be used. As derived in Appendix B, the two transfer functions from the voltage input δU_a^* to the two state variables current δi_a^* and shaft speed $\delta\omega^*$ are:

$$\frac{\delta i_a^*(s)}{\delta U_a^*(s)} = \frac{\left(\tau_{\omega,e}s + 1\right) \cdot \frac{U_{a,0}}{U_{a,0} - K_e\omega_{em,0}}}{\tau_{em}\tau_{\omega,e}s^2 + \left(\tau_{em} + \tau_{\omega,e}\right)s + 1 + \frac{1}{2\eta_{trm}} \cdot \frac{K_e\omega_{em,0}}{U_{a,0} - K_e\omega_{em,0}}} \tag{13}$$

and

$$\frac{\delta\omega^*(s)}{\delta U_a^*(s)} = \frac{\frac{1}{2\eta_{trm}} \cdot \frac{U_{a,0}}{U_{a,0} - K_e\omega_{em,0}}}{\tau_{em}\tau_{\omega,e}s^2 + \left(\tau_{em} + \tau_{\omega,e}\right)s + 1 + \frac{1}{2\eta_{trm}} \cdot \frac{K_e\omega_{em,0}}{U_{a,0} - K_e\omega_{em,0}}} \tag{14}$$

in which $\tau_{\omega,e} \equiv \frac{\tau_{\omega}}{2\eta_{trm}}$. The approximated two poles and DC-gains and the single zero of the two transfer functions are given in Table 2. These expressions will later on be used to estimate system parameter values based on measurements. The derivation of both the exact poles and their approximations is given in Appendix C.

Table 2: Poles, zero and DC-gains of the linearised system

	approximate poles	**zero**	**DC-gains**
$\frac{\delta i_a^*(s)}{\delta U_a^*(s)}$	$s_1 \cong -\frac{C}{\tau_{\omega,e}}$, $s_2 \cong -\frac{1}{\tau_{\text{em}}}$	$\frac{-1}{\tau_{\omega,e}}$	$\frac{2\eta_{trm}U_{a,0}}{2\eta_{trm}R_a i_{a,0} + K_e\omega_{em,0}}$
$\frac{\delta\omega^*(s)}{\delta U_a^*(s)}$	$C \equiv 1 + \frac{1}{2\eta_{trm}} \cdot \frac{K_e\omega_{em,0}}{U_{a,0} - K_e\omega_{em,0}}$	n.a.	$\frac{U_{a,0}}{2\eta_{trm}R_a i_{a,0} + K_e\omega_{em,0}}$

3 Tito Neri system parameter estimation based on earlier work

Earlier work by Sang (2018) gave estimates of the unknown system parameters of the Tito Neri propulsion system. These estimates were based on a combination of steady state tests at various operating points and transients between the various operating points. Initial tests focused on the isolated subsystem of DC-motor and

http://doi.org/10.24868/issn.2631-8741.2018.013

shaft 1. In later tests shaft 2 and 3 plus the propeller were included and experiments in both dry and wet condition were carried out.

Although various simplifications and assumptions had to be made by Sang (2018), the resulting parameter estimates as given in Table 3 are used as a reference to compare system parameters and behaviour as will be obtained via other methods. Striking is the relatively high total friction of the drivetrain, leading to a very low transmission efficiency of around 40%. This might seem to be a mistake, but qualitatively aligns with manual rotation of the shaft during which high friction can be observed. Possible reasons could be the quality of the toy-thruster and its gear wheels and the far from optimal alignment of the shafts in combination with the bearings. As far as can be judged, other values do at least seem of the correct order of magnitude.

Sang (2018) implemented the estimated parameters in a non-linear simulation model based on Eqs. (1) and (3) and compared results with experimentally obtained time domain validation data. Overall the validation was successful, with good agreement of both steady state values and transients of current and motor speed. Some discrepancies in bollard pull force behaviour during transients could be explained by undesired pitching of the ship due to the (too high) connection of the towing line to the ship. Some unexplained phenomena occurred during fast transients of the current. Whether they were physical or caused by undesired sensor behaviour could not be determined. Importantly, they are not expected to have influence on the behaviour of the motor speed.

Table 3: Parameter estimates taken from Sang (2018) plus updated parameter estimates.

	(Sang, 2018) portside	**(Sang, 2018) starboard side**	**Updated starboard estimates (this paper)**
L_a [H]	7.39e-4	5.57e-4	7.59e-4 (+36%)
K_e [NmA^{-1}]	0.018	0.018	0.0156 (-14%)
R_a [Ω]	1.04	0.90	1.21 (+34%)
$I_{p,tot}$ [kgm^{-2}]	2.01e-5	2.00e-5	2.53e-5 (+26%)
M_f [Nm]	1.89e-2	2.29e-2	2.60e-2 (+14%)
$K_{Q,J=0}$ [-]	0.19	0.17	0.11 (-36%)
$K_{T,J=0}$ [-]	0.55	0.53	Not considered
$(1-t)$ [-]	Effect included in K_T	Effect included in K_T	Not considered
η_{trm} [-](derived)	0.42	0.36	0.27 (-25%)
η_{em} [-](derived)	0.71	0.73	0.63 (-14%)
$\eta_{trm} \cdot \eta_{em}$ [-] (derived)	0.30	0.26	0.17 (-35%)
τ_{em} [s] (derived)	7.1e-4	6.2e-4	6.3e-4 (-2%)
τ_{ω} [s] (derived)	0.16	0.15	0.21 (+40%)
$\tau_{\omega,e}$ [s] (derived)	0.19	0.21	0.4 (+90%)

The “starboard” parameters as determined by Sang (2018) as shown in Table 3 are implemented in Eqs. (13) and (14). The resulting predicted behaviour in the frequency domain is visualised in Figure 4 (absolute gain) and Figure 5 (dB gain). At low frequencies the response of shaft speed to voltage is constant, with a DC-gain as described in Table 2, and a phase lag of 0 degrees. Around 25 rad/s (the location of the first pole) the shaft speed response starts to drop with a slope of -20 dB/decade, indicating that the inertia of the drivetrain becomes a dominant factor. The second pole, located around 1600 rad/s and related to the electrical inertia of the system, causes the slope to drop to -40 dB/decade. The phase lag approaches -180 degrees at high frequencies.

The response of current to voltage is shown in the same figure. At low frequencies the response is constant, with a value according to the DC-gain in Table 2. The zero of the transfer function lies around 5 rad/s and pushes the gain upwards with a slope of +20 dB/decade and towards 90 degrees phase lead although it doesn’t reach that

http://doi.org/10.24868/issn.2631-8741.2018.013

phase. Around 25 rad/s the first pole results in a steady gain around 3.5 (or ~10 dB). Around 1600 rad/s the second pole pushes the response downwards with a slope of -20 dB/decade and a phase lag of 90 degrees.

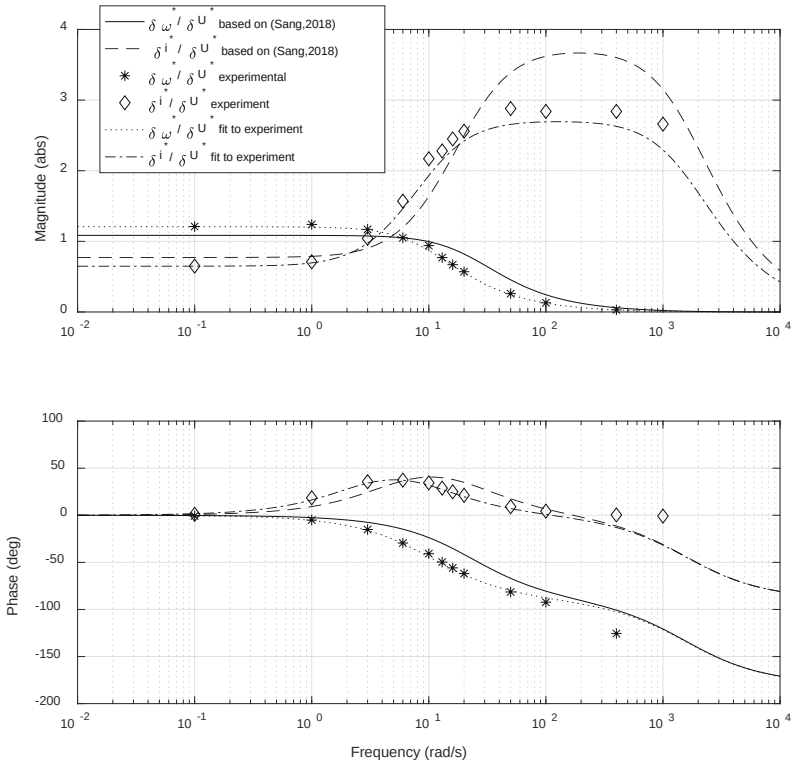

Figure 4: Frequency domain results (starboard drivetrain)

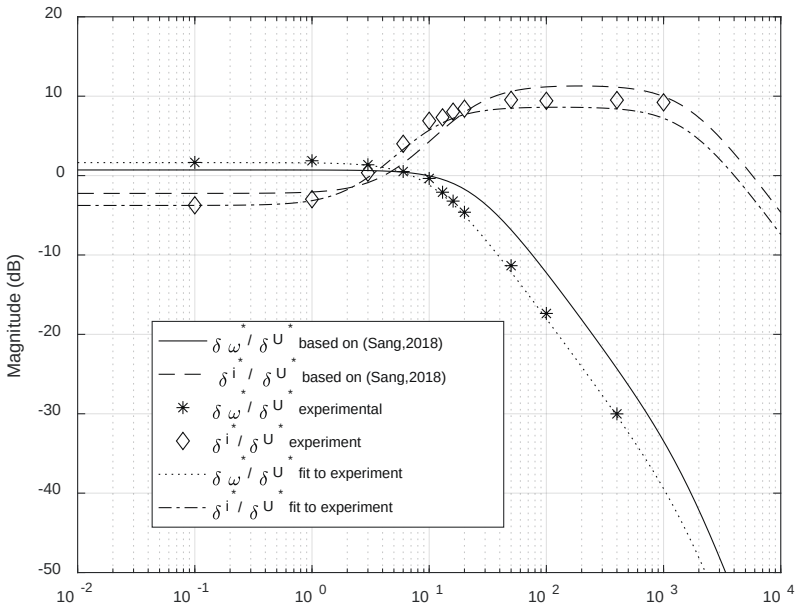

Figure 5: Frequency domain results in dB scale (starboard drivetrain)

http://doi.org/10.24868/issn.2631-8741.2018.013

4 Experimental determination of the frequency domain behaviour

In the previous section the behaviour of the Tito Neri propulsion system in the frequency domain was predicted based on parameters found by Sang (2018) and shown in Figure 4 and Figure 5. In this section the approach that was taken to validate this behaviour is described. The idea of the applied method is to generate a sinusoidal voltage of a specific frequency ω_U and amplitude U_{ampl}, to superimpose it on a constant voltage value $U_{a,0}$, and to apply the resulting signal as a voltage input U_a to the system, while recording the response of current i_a and electric motor speed ω_{em}. Based on the input and output signals at each frequency, the gain and phase of the transfer function of the system is estimated with a correlation based single frequency approach (Balmer 1997), in line with Figure 6.

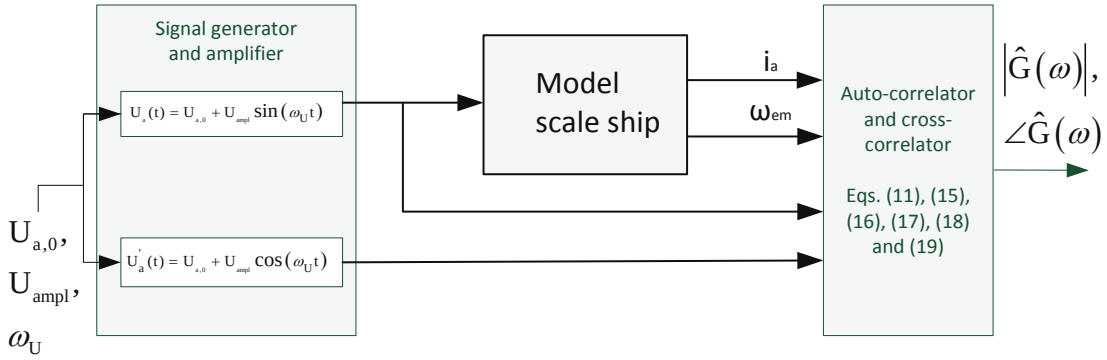

Figure 6: Single frequency testing with the correlation method

The idea of the method is to generate two signals $U_a(t)$ and $U_a^{'}(t)$ of which the first signal is used to excite the system. Subsequently, both signals, in combination with the measurements are used to determine the cross correlations and autocorrelation according to:

$$R_{xy} = \frac{1}{T}\int_0^T X\sin(\omega t)\cdot Y\sin(\omega t+\varphi)dt + R_{xn} = \frac{XY}{2}\cos\varphi + R_{xn} \tag{15}$$

$$R_{x'y} = \frac{1}{T}\int_0^T X\cos(\omega t)\cdot Y\sin(\omega t+\varphi)dt + R_{x'n} = \frac{XY}{2}\sin\varphi + R_{x'n} \tag{16}$$

$$R_{xx} = \frac{1}{T}\int_0^T X\sin(\omega t)\cdot X\sin(\omega t)dt = \frac{X^2}{2} \tag{17}$$

where X is the amplitude of the input signal (in this case the amplitude voltage δU_a^*) and Y is the amplitude of the output signal under consideration (in this case the amplitudes of motor current δi_a^* or motor speed $\delta\omega_{em}^*$). R_{xn} is the cross-correlation between input and noise, which reduces to zero with increasing measurement time.

Division of Eq. (15) by Eq. (17) delivers the in phase (real) component of the frequency response while division of Eq. (16) by Eq. (17) gives the out of phase (imaginary) part of the response:

$$\frac{R_{xy}}{R_{xx}} = \frac{Y}{X}\cos\varphi \text{ and } \frac{R_{x'y}}{R_{xx}} = \frac{Y}{X}\sin\varphi \tag{18}$$

Based on the real and imaginary components the gain and the phase of the transfer function are calculated by:

$$\left|\hat{G}\right| = \frac{Y}{X} = \sqrt{\left(\frac{R_{xy}}{R_{xx}}\right)^2 + \left(\frac{R_{x'y}}{R_{xx}}\right)^2} \text{ and } \angle\hat{G} = \arctan2\left(\frac{R_{x'y}}{R_{xx}}, \frac{R_{xy}}{R_{xx}}\right) \tag{19}$$

By using this approach, the gain and phase can be determined experimentally for a number of frequencies, which results in an estimate of the transfer function G.

Advantages of the method are:

- It is easy to understand and program;

http://doi.org/10.24868/issn.2631-8741.2018.013

- All the power in the input signal is concentrated in a single frequency, which results in good noise immunity;
- Noise immunity increases with measurement time.

Disadvantages of the single frequency method are:

- Because all power is concentrated at a single input frequency, resonances might be excited in the system. When resonances occur this might result in non-linear behaviour or may cause excessive wear or even physical damage. It is however not expected that this will be a problem for the model scale ship under consideration, but should be considered for full scale application.
- Especially for the lower frequencies the required measurement time can be long. This is caused by the required number of cycles per frequency and by the required settling time after each frequency change. Drawback of a long measurement time is that the system operating point can drift. Compared to other approaches the requires time is however still very limited.

To further reduce the measurement time required by the single frequency testing method, multi-frequency testing methods have been developed (Balmer 1997). Such methods require much less total measurement time, but come at the cost of additional processing complexity.

4.1 Results of single harmonic frequency testing

The correlation based single frequency approach as described in the previous section was applied to the model scale ship in bollard pull condition. Besides input voltage, only current and motor speed were measured. The nominal operating point was chosen as $U_{a,0} = 6.5V$ on top of which the sinusoidal voltage variation was superimposed.

In Figure 4 and Figure 5 the experimental estimates of the transfer functions are compared against the linear model, based on parameters obtained by Sang (2018). The steady state gains and phase angles of both transfer functions at frequencies up to 1 rad/s align reasonably well, although differences do exist.

A difference is the value of the maximum gain of the current response between 50-500 rad/s. The linearised model predicts a gain of 3.5, while the experiments give a gain of 2.9. On a dB scale the difference is less obvious.

Another difference is the frequency at which the shaft speed response starts to drop. According to the linear model and the Sang (2018) parameter-set, the pole lies around 25 rad/s, but the experimentally determined gain and phase seem to suggest that this pole should lie slightly to the left.

A possible explanation of the differences could be the 1 year time difference between the measurements by Sang (2018) and the measurements that were made particularly for this paper. During this year the parameters of the system (especially the friction/ transmission efficiency) might easily have changed. Another reason might lie in the calibration of the current sensor, which was not carried out according to the same procedure each time.

Nevertheless, despite the differences, the overall shape of the transfer functions aligns well. Due to limitations of the amplifier and the current sensor, measurements at frequencies higher than shown in the graphs were not meaningful and are not presented.

Note that all data points are corrected for (measured) reduced gain and phase lag introduced by the amplifier that have been experimentally determined as well. This correction improved the results slightly, especially at the data points at 1000 and 500 rad/s, where the effect of the undesired dynamics of the amplifier started to play a role.

4.2 Parameter estimation based on experimentally obtained frequency domain behaviour

As an alternative for the parameter estimation method as described by Sang (2018), it is possible to estimate the unknown (or at least uncertain) system parameters based on the data points in the frequency domain as obtained with the correlation based single frequency approach.

The least advanced method to carry out such estimation is to read the experimentally observed DC-gains, the estimated pole locations and the zero location from Figure 4 and Figure 5. In combination with the (approximate) analytical solutions as given in Table 2, this leads to 5 equations with 5 unknowns.

The transmission efficiency (and therewith indirectly the friction M_f) can for instance be estimated by taking the ratio between the experimentally observed DC gains from the Bode plot. Subsequently the observed location of the first pole can be used to estimate K_e. With estimated values of η_{trm} and K_e the resistance R_a can be estimated via the DC-gains. Finally inductance L_a can be estimated given R_a and the experimentally identified location of the second pole. Although very simple, this approach leads to a set of estimated parameters that, once applied in system (12) fits the measured frequency domain data points very well, as shown in Figure 4 and

 http://doi.org/10.24868/issn.2631-8741.2018.013

Figure 5. For reference the updated estimated parameter values are shown in the right column of Table 3. Although the values differ from the results found by Sang (2018), they are still in the same range, which gives confidence in the approach.

The main advantage of the fitting approach via the frequency domain compared to the approach by Sang (2018) is that, through the use of the correlation method, the effect of noise is mitigated. A requirement however is that the poles and zero(s) are clearly recognisable from the experimental results, which requires both sufficient frequency resolution and sufficient separation between poles and zeros. In the example the second pole (expected around 1600rad/s) is not recognisable from experiments, which affects the estimate of inductance L_a. In cases where these requirements are not met, fitting methods that take into account more (preferably all) experimental data points are required. Such methods are readily available in for instance the System Identification Toolbox of MATLAB ©.

Finally note that it is not a requirement that the frequency domain behaviour was obtained with the single frequency correlation method as described before: another method could be to apply multi-frequency testing in order to decrease testing time (Balmer, 1997). Yet another approach could be to use random input signal testing, which is a topic of further study.

5 Future work

The application of parameter identification techniques on the propulsion plant of an educational model scale boat in itself is instructive. It shows how (linear) system and control theory can be applied in a maritime setting, both in a theoretical and in an experimental way.

Although linear models have their limitations, and although the demonstrated methods have thus far only been applied on model scale, the authors believe that a similar approach could be worthwhile to develop further and test on full scale. Typically modelling of a ship (propulsion) plant is a laborious task, not in the least because parameters are not always "known" or easy to determine. In such a case the introduced identification techniques could offer benefit, especially considering that the required testing time is limited and can for instance be combined with required sea acceptance trials such as the bollard pull test or endurance test. If such an approach works, a periodic repeat of the test can be considered, which potentially could reveal change of parameters which subsequently might point at component degradation. This could be seen as taking a periodic "fingerprint" of the system.

It is important to realise that on full scale a number of differences have to be taken into consideration. First of all, assuming a diesel driven full scale ship, the dynamic model and thus the transfer functions are different from what is reported in this paper, but instead follow the derivations given by Stapersma and Vrijdag (2017) and Vrijdag and Stapersma (2017), of which the latter includes the dynamics of the diesel engine governor. Due to the high full scale ship mass and polar moment of inertia compared to model scale, and the additional dynamics of the governor, the lowest frequencies of interest shift to lower values, meaning that testing at full scale takes longer compared to model scale.

A second difference is that on model scale, the input is supply voltage, while on full scale the most convenient inputs are the "engine speed setpoint", which is an input into the governor, and in case of a CPP the "propeller pitch setpoint", which is an input into the (local) propeller pitch controller. Possible ways to excite the system could include additional "fingerprinting" software in the engine governor and/or pitch controller, which would require cooperation of the supplier. Another approach could be to use the external inputs of the controllers (ie. a 4-20mA engine speed setpoint input, but other options exist dependent on the manufacturer) to feed in a sinusoidal signal including DC offset generated by a (handheld) signal generator.

Thirdly there are dynamic effects, some of which non-linear, which are not modelled in the linear model by Vrijdag and Stapersma (2017), but which should be taken into consideration. Dependent on the goals of the identification test, the curvature in the open water diagram and in the resistance curve, might for instance force the user to "fingerprint" at various nominal operating points. Another type of non-linearity is introduced by the discrete nature of the diesel engine combustion and air exchange process, which puts an ignition frequency related upper limit to a meaningful excitation frequency. The discrete nature of the local controller behaviour also has an effect on the highest meaningful excitation frequency. Yet another effect, briefly mentioned earlier, that should be taken into account when planning full scale experiments, is the possibility that an introduced excitation frequency might cause (rotational) resonance in the drive system, thereby possibly causing excessive wear and even damage of for instance the gears or the flexible coupling. Whether this is a real risk needs to be determined on a case by case basis, and if so, such excitation frequencies should be avoided or only be used with small amplitude.

http://doi.org/10.24868/issn.2631-8741.2018.013

Main limitation of the approach demonstrated in this paper is that it cannot deal with strong non-linear behaviour such as for example introduced by (rate) limiting features implemented in the diesel engine speed governor and introduced by for instance the CPP mechanism. The result of the governor-engine-limit example is that a nominal operating point that lies too close to the engine operating envelope should not be selected for application of linear identification techniques.

6 Conclusions and recommendations

In this paper a parameter identification technique is applied on a model scale ship in bollard pull conditions and results are compared with earlier work by Sang (2018). Results are very similar, and the differences are most likely caused by changes of system friction over the course of more than one year and/or differences in calibration procedure of the current sensor.

As part of the identification procedure a linear model of the propulsion system has been derived, which could be validated with experiments. This can be seen as the first (partial) experimental validation of the linearised model as was set up by Stapersma and Vrijdag (2017) and Vrijdag and Stapersma (2017), although modifications had to be made to the linearised model to make it applicable for the DC-motor driven model scale ship.

There are various possible directions in which this work can be extended in the future. First of all the current model scale setup can be improved. Improvements can be made to the connection of the towing line to the ship, which in this case turned out to be positioned too high leading to a pitching moment. Another recommended improvement is to use a current sensor that is less sensitive to temperature and that gives less noisy measurements.

Another possible direction is to extend the application of identification techniques towards free sailing ship models, thereby including the resistance curve and the open water diagram into the system. One of the practical difficulties in that case is to wirelessly operate the ship, while logging measurement data and keeping the ship within the boundaries of the towing tank or flume tank.

Considering the application on full scale there is more work to be done. The authors however believe that such experiments could be a valuable stepping stone for ship system integrators towards having full understanding of (and control over) dynamic ship propulsion system behaviour.

Summarising: it is concluded that the parameter identification by making use of a short “rich” test cycle was low hanging fruit for the model scale ship in bollard pull conditions. Further work is required to see whether the ideas can be extended to full scale application.

Regardless whether model scale or full scale, bollard pull condition or free sailing condition is considered, the availability of both the non-linear and linearised model opens up the possibility to make use of a wealth of existing tools and methods coming from the field of systems and control, which have found limited application in a ship propulsion related setting before.

7 Acknowledgements

The work reported in this paper had not been possible without the assistance of Vittorio Garafano (DUT) during all experiments. Furthermore, the authors wish to acknowledge the support of Dr. Milinko Godjevac (DUT) and Dr. Michele Martelli (Genova University). Their support during experimentation and discussion of the results during the MSc. thesis project of mr. Yueming Sang is much appreciated.

8 References

Balmer, L. (1997) *Signals and Systems: An Introduction,* 2nd ed., Prentice Hall.

Carlton, J. (2007) *Marine Propellers and Propulsion,* Elsevier Butterworth-Heinemann.

Cipollini, F., Oneto, L., Coraddu, A., Murphy, A. J. and Anguita, D. (2018) Condition-Based Maintenance of Naval Propulsion Systems with supervised Data Analysis. *Ocean engineering, 149*, pp. 268-278.

Coraddu, A., Oneto, L., Ghio, A., Savio, S., Anguita, D. and Figari, M. (2016) Machine learning approaches for improving condition-based maintenance of naval propulsion plants. *Proceedings of the Institution of Mechanical Engineers Part M-Journal of Engineering for the Maritime Environment, 230*(1), pp. 136-153.

 http://doi.org/10.24868/issn.2631-8741.2018.013

Geertsma, R. D., Negenborn, R. R., Visser, K., Loonstijn, M. A. and Hopman, J. J. (2017) Pitch control for ships with diesel mechanical and hybrid propulsion: Modelling, validation and performance quantification. *Applied Energy, 206*, pp. 1609-1631.

Martelli, M. and Figari, M. (2017) Real-Time model-based design for CODLAG propulsion control strategies. *Ocean engineering, 141*, pp. 265-276.

Mizythras, P., Boulougouris, E. and Theotokatos, G. (2018) Numerical study of propulsion system performance during ship acceleration. *Ocean engineering, 149*, pp. 383-396.

Sang, Y. (2018) *Parameter Identification, Simulation, Linearization and Validation of a Ship Propulsion System*. Unpublished MSc, Delft University of Technology.

Stapersma, D. and Vrijdag, A. (2017) Linearisation of a ship propulsion system model. *Ocean engineering, 142*, pp. 441-457.

Vrijdag, A. and Stapersma, D. (2017) Extension and application of a linearised ship propulsion system model. *Ocean engineering, 143*, pp. 50-65.

Vrijdag, A., Stapersma, D. and van Terwisga, T. (2009) Systematic modelling, verification, calibration and validation of a ship propulsion simulation model. *Journal of Marine Engineering & Technology*, *8*(3), pp. 3-20.

Nomenclature

B	beam	R_{xx}	autocorrelation
D	propeller diameter	R_{xy}	cross correlation
F_{BP}	bollard pull force	s	Laplace operator
I_p	polar moment of inertia	T	draft
i_a	current	T	period
i_{gb}	gearbox ratio	t	time
K_e	motor constant	t	thrust deduction factor
K_Q	propeller torque coefficient	U_a	supply voltage
K_T	propeller thrust coefficient	X	input signal amplitude
k_p	number of propellers	Y	output signal amplitude
L_{oa}	length overall		
L_a	inductance		
$M_{b,\epsilon}$	brake motor torque	Δ	displacement
M_f	friction torque	η	efficiency
M_p	propeller torque	ρ	Water density

http://doi.org/10.24868/issn.2631-8741.2018.013

n_p	propeller speed	τ	Integration constant, time constant
n	noise	φ	Phase angle
Q	open water propeller torque	ω	Angular speed
R_a	resistance		

Appendix A Linearised and normalised differential equations

Appendix A.1 Electrical circuit dynamics

The electric circuit dynamics of the DC motor are modelled by:

$$L_a \frac{di_a}{dt} = U_a - K_e \omega_{em} - R_a i_a \tag{A-1}$$

All three right hand side terms vary around equilibrium:

$$U_a = U_{a,0} + \delta U_a, \qquad K_e \omega_{em} = K_e \left(\omega_{em,0} + \delta \omega_{em} \right), \qquad R_a i_a = R_a \left(i_{a,0} + \delta i_a \right) \tag{A-2}$$

In static conditions the right hand side of Eq. (A-1) equals zero:

$$0 = U_{a,0} - K_e \omega_{em,0} - R_a i_{a,0} \tag{A-3}$$

Substitution of Eq. (A-2) into Eq. (A-1) and then subtracting Eq. (A-3) shows that only the small increments are of importance:

$$L_a \frac{di_a}{dt} = \delta U_a - K_e \delta \omega_{em} - R_a \delta i_a \tag{A-4}$$

Division of all terms by nominal supply voltage minus the nominal emf $\left(U_{a,0} - K_e \omega_{em,0} \right)$ or by its equivalent $R_a i_{a,0}$ gives:

$$\frac{L_a}{R_a i_{a,0}} \cdot \frac{di_a}{dt} = \frac{1}{U_{a,0} - K_e \omega_{em,0}} \cdot \frac{U_{a,0}}{U_{a,0}} \delta U_a - \frac{K_e}{U_{a,0} - K_e \omega_{em,0}} \cdot \frac{\omega_{em,0}}{\omega_{em,0}} \delta \omega_{em} - \frac{R_a}{R_a i_{a,0}} \delta i_a \tag{A-5}$$

With some simplifications this equals:

$$\tau_{em} \frac{di_a^*}{dt} = \frac{U_{a,0}}{U_{a,0} - K_e \omega_{em,0}} \delta U_a^* - \frac{K_e \omega_{em,0}}{U_{a,0} - K_e \omega_{em,0}} \delta \omega^* - \delta i_a^* \tag{A-6}$$

in which the subscript $_{\text{em}}$ is intentionally dropped from $\delta \omega_{em}^*$ because $\delta \omega_{em}^* = \delta \omega_p^*$ and where:

$$\tau_{em} \equiv \frac{L_a}{R_a} \tag{A-7}$$

Note that the electric motor efficiency is defined as:

$$\eta_{em} = \frac{P_{out}}{P_{in}} = \frac{K_e i_a \omega_e}{U_a i_a} = \frac{K_e \omega_e}{U_a} \tag{A-8}$$

Appendix A.2 Shaft dynamics

The shaft dynamics, including constant friction term, are described by:

$$I_{p,tot} \frac{d\omega_{em}}{dt} = M_{b,em} - M_f - \frac{M_p}{i_{gb,13}} \tag{A-9}$$

in which shaft inertia is assumed constant implying that change of mass of water, entrained by the propeller, is neglected. The brake motor torque is related to current by:

$$M_{b,em} = K_e \cdot i_a \tag{A-10}$$

The non-constant torque-terms vary around equilibrium:

http://doi.org/10.24868/issn.2631-8741.2018.013

$$M_{b,em} = M_{b,em,0} + \delta M_{b,em} = K_e \left(i_{a,0} + \delta i_a \right) \tag{A-11}$$

and

$$M_p = M_{p,0} + \delta M_p \tag{A-12}$$

such that:

$$I_{p,tot} \frac{d\omega_{em}}{dt} = K_e \left(i_{a,0} + \delta i_a \right) - M_f - \frac{M_{p,0}}{i_{gb,13}} - \frac{\delta M_p}{i_{gb,13}} \tag{A-13}$$

In steady nominal condition the driving torque and the load-torque are equal:

$$0 = K_e i_{a,0} - M_f - \frac{M_{p,0}}{i_{gb,13}} \tag{A-14}$$

Subtracting Eq. (A-14) from Eq. (A-13) shows that only the small increments are of importance:

$$I_{p,tot} \frac{d\omega_{em}}{dt} = K_e \delta i_a - \frac{\delta M_p}{i_{gb,13}} \tag{A-15}$$

Normalising all terms with nominal motor torque gives:

$$\frac{I_{p,tot}\omega_{em,0}}{K_e i_{a,0}} \frac{d\omega^*}{dt} = \delta i_a^* - \frac{M_{p,0}}{M_{b,em,0} i_{gb,13}} \delta M_p^* \tag{A-16}$$

in which the subscript $_{em}$ is intentionally dropped from $\delta\omega_{em}^*$ because $\delta\omega_{em}^* = \delta\omega_p^*$. The integration constant is defined as:

$$\tau_\omega \equiv \frac{I_{p,tot}\omega_{em,0}}{M_{b,em,0}} \equiv \frac{I_{p,tot}\omega_{em,0}}{K_e \cdot i_{a,0}} \tag{A-17}$$

After noting that the multiplier in the second term of the right hand side of (A-16) can be written as:

$$\frac{M_{p,0}}{i_{gb,13} M_{b,em,0}} = \eta_{trm} \tag{A-18}$$

and implementing

$$\delta M_p^* = 2\delta\omega^* \tag{A-19}$$

the normalised linearised differential equation for shaft speed is given by:

$$\tau_\omega \frac{d\omega^*}{dt} = \delta i_a^* - 2\eta_{trm}\delta\omega^* \tag{A-20}$$

Appendix B *Laplace transfer functions*

Starting with the differential Eq. (A-20) for shaft rotation the Laplace operator is introduced which gives:

$$\tau_\omega s\delta\omega^* = \delta i_a^* - 2\eta_{trm}\delta\omega^* \tag{B-1}$$

Introducing the equation for DC-motor torque, and re-arranging gives:

$$\left(\frac{\tau_\omega}{2\eta_{trm}} s + 1 \right) \delta\omega^* = \frac{1}{2\eta_{trm}} \delta i_a^* \tag{B-2}$$

which can be shortened by introduction of the effective time-constant $\tau_{\omega,e} \equiv \frac{\tau_\omega}{2\eta_{trm}}$:

$$\left(\tau_{\omega,e} s + 1 \right) \delta\omega^* = \frac{1}{2\eta_{trm}} \delta i_a^* \tag{B-3}$$

Similarly, introduction of the Laplace operator in the differential equation for current Eq. (A-6) gives:

$$\left(\tau_{em} s + 1 \right) \delta i_a^* = \frac{U_{a,0}}{U_{a,0} - K_e\omega_{em,0}} \delta U_a^* - \frac{K_e\omega_{em,0}}{U_{a,0} - K_e\omega_{em,0}} \delta\omega^* \tag{B-4}$$

http://doi.org/10.24868/issn.2631-8741.2018.013

Appendix B.1 Transfer function from supply voltage to rotation speed

Reordering of Eq. (B-4) gives:

$$\delta i_a^* = \frac{\left(\frac{U_{a,0}}{U_{a,0} - K_e\omega_{em,0}}\right)}{\left(\tau_{em}s+1\right)}\delta U_a^* - \frac{\left(\frac{K_e\omega_{em,0}}{U_{a,0} - K_e\omega_{em,0}}\right)}{\left(\tau_{em}s+1\right)}\delta\omega^* \tag{B-5}$$

Substitution of Eq. (B-5) into Eq. (B-3) gives:

$$\left(\tau_{\omega,e}s+1\right)\delta\omega^* = \frac{1}{2\eta_{trm}}\left(\frac{\left(\frac{U_{a,0}}{U_{a,0} - K_e\omega_{em,0}}\right)}{\left(\tau_{em}s+1\right)}\delta U_a^* - \frac{\left(\frac{K_e\omega_{em,0}}{U_{a,0} - K_e\omega_{em,0}}\right)}{\left(\tau_{em}s+1\right)}\delta\omega^*\right) \tag{B-6}$$

Reordering gives the transfer function:

$$\frac{\delta\omega^*}{\delta U_a^*} = \frac{\frac{1}{2\eta_{trm}}\cdot\frac{U_{a,0}}{U_{a,0} - K_e\omega_{em,0}}}{\tau_{em}\tau_{\omega,e}s^2 + \left(\tau_{em}+\tau_{\omega,e}\right)s + 1 + \frac{1}{2\eta_{trm}}\cdot\frac{K_e\omega_{em,0}}{U_{a,0} - K_e\omega_{em,0}}} \tag{B-7}$$

Appendix B.2 Transfer function from supply voltage to current

In a similar way substitution of Eq.(B-3) into Eq. (B-4) and reordering gives:

$$\frac{\delta i_a^*}{\delta U_a^*} = \frac{\left(\tau_{\omega,e}s+1\right)\cdot\frac{U_{a,0}}{U_{a,0} - K_e\omega_{em,0}}}{\tau_{em}\tau_{\omega,e}s^2 + \left(\tau_{em}+\tau_{\omega,e}\right)s + 1 + \frac{1}{2\eta_{trm}}\cdot\frac{K_e\omega_{em,0}}{U_{a,0} - K_e\omega_{em,0}}} \tag{B-8}$$

Appendix C *Derivation of exact system poles and their approximations*

The characteristic equation of the two transfer functions (B-7) and (B-8) is given by:

$$\tau_{em}\tau_{\omega,e}s^2 + \left(\tau_{em}+\tau_{\omega,e}\right)s + 1 + \frac{1}{2\eta_{trm}}\cdot\frac{K_e\omega_{em,0}}{U_{a,0} - K_e\omega_{em,0}} \tag{C-1}$$

If we define:

$$C \equiv 1 + \frac{1}{2\eta_{trm}}\cdot\frac{K_e\omega_{em,0}}{U_{a,0} - K_e\omega_{em,0}} \tag{C-2}$$

and

$$\zeta \equiv \frac{\tau_{em}}{\tau_{\omega,e}} \tag{C-3}$$

then Eq. (C-1) can be written as:

$$\zeta\tau_{\omega,e}s^2 + \left(1+\zeta\right)s + \frac{C}{\tau_{\omega,e}} \tag{C-4}$$

The two exact roots of Eq. (C-4) can be determined by the ABC formula:

$$s = \frac{-\left(1+\zeta\right) \pm \sqrt{\left(1+\zeta\right)^2 - 4C\zeta}}{2\zeta\tau_{\omega,e}} \tag{C-5}$$

which can be written as:

http://doi.org/10.24868/issn.2631-8741.2018.013

$$s = \frac{-(1+\zeta) \pm (1+\zeta)\sqrt{1-\frac{4C\zeta}{(1+\zeta)^2}}}{2\zeta\tau_{\omega,e}} \tag{C-6}$$

The electrical time constant is much smaller than the effective time constant for the shaft, therefore $\zeta \ll 1$. Application of Taylor expansion for the square root operation and leaving out second order terms gives:

$$s \cong \frac{-(1+\zeta) \pm (1+\zeta)\cdot\left(1-2C\zeta\cdot\frac{1}{(1+\zeta)^2}\ldots\right)}{2\zeta\tau_{\omega,e}} \tag{C-7}$$

Another Taylor expansion for the inverse square operation gives:

$$s \cong \frac{-(1+\zeta) \pm (1+\zeta)\cdot(1-2C\zeta\cdot(1-2\zeta\ldots)\ldots)}{2\zeta\tau_{\omega,e}} \tag{C-8}$$

Further simplification gives the two approximate poles as:

$$s_1 \cong \frac{-C}{\tau_{\omega,e}} \tag{C-9}$$

and

$$s_2 \cong \frac{-1}{\zeta\tau_{\omega,e}} = \frac{-1}{\tau_{em}} \tag{C-10}$$

http://doi.org/10.24868/issn.2631-8741.2018.013